Influence of environmental temperature and device temperature difference on output parameters of c-Si solar cells

Xiaodong Lu *, Yang Zhao, Zelai Wang, Jinjing Zhang, Yang Song

College of New Energy, Bohai University, Jinzhou, Liaoning 121000, China

ARTICLE INFO

ABSTRACT

Influence of environmental temperature and the temperature difference between the front and back surfaces of the cell on the output parameters of a typical commercial c-Si solar cell is analyzed by two-dimensional finite difference method. The results show that even for the cell with its front and back surfaces at the same temperature, the temperature distribution in the cell's interior is not homogeneous; the temperature difference between the front and back surfaces will generate a temperature gradient inside the cell; the temperature variation in the cell's interior for both the front and back surfaces at the same and different temperature can be divided into two regions; considering three heat mechanisms related with carrier transport process, Peltier and Thomson effects and Joule heat effects have more important influences on the temperature; with environmental temperature increasing, the values of open circuit voltage, fill factor and efficiency will all decrease and those of short current will increase; with the temperature difference increasing, the values of $|J_{sc}|$ and FF will decrease, but those of V_{oc} and η will increase.

© 2016 Elsevier Ltd. All rights reserved.

1. Introduction

Crystalline silicon (c-Si) solar cells (SCs), which are the dominant products in the photovoltaic market, have been widely used to satisfy the electrical energy needs under various environmental conditions, including some extreme environmental conditions, such as high mountains, inhospitable deserts or islands in various latitudes. Due to the sensitivity of the c-Si material to environmental temperature, the output parameters of c-Si SCs will vary greatly in different environmental conditions. Therefore, the studies on the output parameters of c-Si SCs varying with temperature are very important for further extending their application ranges and predicting the output power of a photovoltaic (PV) system (Agarwala et al., 1980).

Researchers have paid much attention to investigating how the output parameters of c-Si SCs vary with temperature. The early results show that (Agarwala et al., 1980; Wysocki and Rappaport, 1960; Fan, 1986; Veissid et al., 1995) with the operating temperature of a c-Si SC increasing, the short current (J_{sc}) remains virtually unchanged and the open circuit voltage (V_{oc}), fill factor (FF) and efficiency (η) all decrease. During the past ten years, PV technologies have received heightened attention worldwide with the global PV installed capacity increasing substantially; the studies on the

changes of the output parameters of c-Si SCs with temperature have gradually become a hot research area in the solar PV field. In 2003, Green has shown theoretically that the performances of c-Si SCs generally decrease with increasing temperature, fundamentally due to increased internal carrier recombination rates, caused by increased carrier concentrations (Green, 2003). In 2005, David et al. have studied both theoretically and experimentally that at a relatively high temperature (around 100–200 °C), the excessive heat in a PV system can be used to increase the total efficiency of solar energy utilization, taking account of the different carrier transport mechanisms and recombination parameters of the cell material (David et al., 2005). In 2008, Singh et al. have investigated that the rate of decrease of V_{oc} with temperature is controlled by the values of the band gap energy, shunt resistance and their rates of change with temperature (Singh et al., 2008). In 2012, Singh and Ravindra have further indicated that the reverse saturation current density has important effects on the efficiency of a c-Si SC varying with temperature (Singh and Ravindra, 2012). In 2014, Xiao et al. show that at high temperature, compensated c-Si SCs can generate more electricity than the conventional c-Si SCs, due to the lower temperature-variation of the minority electron mobility in compensated silicon (Xiao et al., 2014). In 2015, Ghani et al. have investigated that temperature affects each of the five characterization parameters required to characterize their electrical behavior by using the single diode five parameter model and obtained that the reverse saturation current is the most

temperature sensitive characterization parameter (Ghani et al., 2015). These results show that the influence of temperature on the output parameters of c-Si SCs is related with the variations of the basic properties of c-Si materials with temperature.

Diode models are the most commonly used method to establish the relationships between environmental temperature and the output parameters of c-Si SCs (Agarwala et al., 1980; Fan, 1986; Green, 2003; David et al., 2005; Singh et al., 2008; Singh and Ravindra, 2012). For various diode models, there exists the same assumption that the temperature distribution is uniform, but in practical application, the temperature distribution of a c-Si SC will be inevitably influenced by environmental conditions, such as wind speed and solar radiation levels. Several researchers have indicated that a 1.5–3 K temperature difference (T_D) exists between the front and back surfaces (FBSs) of a c-Si SC during its normal operation process (Hosseini et al., 2011; Armstrong and Hurley, 2010; Indartono et al., 2015). In addition, three thermal mechanisms related to carrier transport process will also affect the temperature distribution of a c-Si SC. Therefore, diode model can only be considered as a good approximation to the actual operation situation of a c-Si SC.

Because many facts can affect the temperature distribution of a c-Si SC, its temperature distribution is essentially a spatial non-uniform temperature distribution. The spatial non-uniformity will pose a significant challenge in accurately testing the output parameters of a c-Si SC under different testing conditions, which usually specify that the temperature of the device under test (DUT) must be definite (for example the DUT is specified as 25 ± 1 °C under the Standard Testing Conditions (STC) of SCs). The exact simulation of the temperature distribution for a c-Si SC can help a lot to understand and correct the errors appearing in testing its output parameters under STC or other temperature conditions. In this paper, we will investigate the influences of the temperature non-uniformity on the output parameters of a typical commercial c-Si SC by solving Maxwell equations, stationary semiconductor device equations and heat flow equations by two-dimensional finite difference method. In our simulation, the temperature distributions and temperature gradients (T_gs) inside a c-Si solar cell are first obtained at the different temperatures and then the influences of these mechanisms on T_g values are further analyzed by comparing the heat released and absorbed by different thermal mechanisms. Finally the influences of T_g on the output parameters of the c-Si SC are discussed in detail.

2. Numerical method and cell structure

2.1. Numerical method

Two-dimensional finite difference method is used to solve Maxwell equations, stationary semiconductor device equations and heat flow equations, where the mesh technology are same in solving these equations. A detailed flowchart can be seen in Appendix. The finite difference frequency domain method is first used to solve Maxwell equations and obtain the steady-state distribution of optical intensity in the c-Si SC (Lu et al., 2013) and then the steady-state distribution of carrier-generation rate, which can be viewed as a constant charge source, is obtained by transforming the steady-state distribution of optical intensity (Chao et al., 2010). By introducing the charge source into the Poisson equation and temperature variable into the properties of c-Si material, the semiconductor device equations can be solved by enriched residual free bubble method proposed by Simpson et al. (2012). Finally, the temperature distribution of the c-Si SC and the heat absorbed and released by different mechanisms can be obtained by (https://en.wikipedia.org/wiki/Heat_equation)

$$C\frac{\partial T}{\partial t} = \nabla(\kappa\nabla T) + Q_{thermal} \tag{1}$$

where κ is the thermal conductivity, C is the heat capacity per unit volume and $Q_{thermal}$ denotes the heat generated per unit volume, which can be rewritten as (Ahmad and Gunther, 2004),

$$Q_{thermal} = \left(\frac{J_n^2}{qn\mu_n} + \frac{J_p^2}{qn\mu_p}\right) + \frac{R-G}{q} \cdot [(E_p - E_n) + T(P_n + P_p)] - \frac{T(J_n\nabla P_n - J_p\nabla P_p)}{q} \tag{2}$$

In Eqs. (1) and (2), the values of κ and C at different temperatures are from the website http://www.ioffe.ru/SVA/NSM/Semicond/Si/thermal.html and Glazov and Pashinkin (2001); q is unit charge; n and p denote the electron and hole concentrations, respectively; T is Kelvin temperature; J_n, J_p, μ_n and μ_p are the current densities and mobilities of electrons and holes, respectively; R and G are the carrier generation and recombination rates, respectively; E_n and E_p is the quasi-Fermi levels for electrons and holes, respectively; P_n and P_p are the thermoelectric powers for electron and hole, respectively. In Eq. (2), the first, second and third terms represent Joule heat (Q_J), heat absorbed or released in the generation and recombination process of carriers (Q_C) and heat generated by Peltier and Thomson effects (Q_{PT}), respectively.

In the finite difference method, the material properties and field parameters are defined at the different discrete grid points, in order to accurately resolve these properties and parameters, grid resolution, which is defined as the distance between a grid point and its neighbor, must be small enough, but excessively small resolution will increase greatly the computational burden. In general, the grid resolutions in c-Si SC simulations are often chosen to be on the order of $\lambda_{min}/40$ to $\lambda_{min}/10$, where λ_{min} denotes the minimum absorption wavelength of c-Si material.

2.2. Cell structure and its parameters

As shown in Fig. 1, a typical commercial c-Si SC structure mainly consists of Ag cathode, SiN$_x$ anti-reflection coating (ARC), textured pyramid, c-Si active layer and Al anode on its back surface (Al BR). In Fig. 1, the thickness of c-Si active layer is denoted by $T + H$, where H is the height of pyramid; the layer thicknesses of Ag cathode, ARC and Al BR are denoted by $t1$, $t2$ and $t3$, respectively; the widths of periodically textured structure and Ag cathode are denoted by $w1$ and $w2$, respectively; the textured angle is denoted by θ. Here, we select that $H = 7$ μm, $T = 200$ μm, $t1 = 0.5$ μm, $t2 = 70$ nm, $t3 = 0.5$ μm, $w1 = 10$ μm, $w2 = 0.5$ μm and $\theta = 54.74°$, respectively. In this structure, ARC, periodically textured structure and Al BR form an effective light trapping structure.

In order to decrease the numerical errors arising from the finite-difference approximations, we adopt Yee grid resolution in both X and Y directions as one twentieth of the minimum absorption
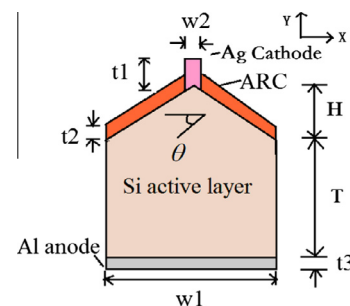

Fig. 1. A typical commercial c-Si SC structure.

wavelength (i.e.300 nm for c-Si material). In our calculation, we assume that the substrate is a p-type c-Si wafer with a uniform doping concentration equal to 7×10^{16} cm^{-3} ($\rho = 0.266$ Ω cm) and the lifetime of minority carriers is equal to 1 ms; the PN junction with the junction depth equal to 0.358 μm is fabricated by traditional phosphorus diffusion process and the impurity profile follows Gaussian distribution with its surface concentration equal to 10^{20} cm^{-3}; good ohmic contacts have been formed between the active layer and two electrodes. In our simulation, the relationships between temperature and the properties of c-Si material adopt the following equations (Ahmad and Gunther, 2004; Madra, 2004; Slotboom, 1977),

$$E_g(T) = E_g(300) + E_{g\alpha} \times \left[\frac{300^2}{300 + E_{g\beta}} - \frac{T^2}{T + E_{g\beta}} \right] \qquad (3)$$

$$N_{c,v}(T) = \left(\frac{T}{300} \right)^{\frac{3}{2}} N_{c,v\_300} \qquad (4)$$

$$\mu_{n,p} = \mu_{n1,p1} \left(\frac{T}{300} \right)^{\alpha_n,\alpha_p} + \frac{\mu_{n2,p2} \left(\frac{T}{300} \right)^{\beta_n,\beta_p}}{1 + \frac{N_d}{N_{n0,p0} \left(\frac{T}{300} \right)^{\gamma_n,\gamma_p}}} \qquad (5)$$

where $E_g(300)$ is the width of band gap; μ_n and μ_p are the electron and hole mobilities, respectively; N_{c_300} and N_{v_300} are the effective state densities of the conduction and valence band at 300 K, respectively; T and N_d are Kelvin temperature and doping concentration, respectively. These parameters are chosen as (Slotboom, 1977; Albrecht et al., 1998; Lycoudes and Childers, 1980): $E_g(300)$ = 1.08 eV, $E_{g\alpha} = 4.73 \times 10^{-4}$, $E_{g\beta} = 636$, $N_{c\_300} = 2.8 \times 10^{19}$ cm^{-3}, $N_{v\_300} = 1.04 \times 10^{19}$ cm^{-3}, $\mu_{n1} = 88$ cm^2/(V s), $\mu_{p1} = 54.3$ cm^2/(V s), $\gamma_n = \gamma_p = 2.546$, $\alpha_n = \alpha_p = -0.57$, $\beta_n = \beta_p = -2.33$, $\mu_{n2} = 1252$ cm^2/(V s), $\mu_{p2} = 407$ cm^2/(V s), $N_{n0} = 1.432 \times 10^{17}$ cm^{-3}, $N_{p0} = 2.67 \times 10^{17}$ cm^{-3}, respectively.

3. Results and discussion

3.1. The influences of T_D and thermal mechanisms on the temperature distribution and T_g

3.1.1. The temperature distributions of the c-Si SC under different temperature conditions

The temperature distribution of a c-Si SC is a comprehensive response of the c-Si SC to environmental temperature, T_d between FBSs and different thermal mechanisms. Fig. 2 gives the temperature distributions of the c-Si SC (as shown in Fig. 1) under different temperature conditions. As shown in Fig. 2, when the FBSs of the c-Si SC have the same temperature, a low-temperature region will appear in very nearly the same position, which lies between 16 μm and 20 μm in the Y direction; when the temperature of the front surface is larger than that of the back surface, a low temperature region appears at the bottom of the cell; the temperature values along the lines parallel to the X-axis are same inside the cell; The temperature variations in Fig. 2(a) and (b) are very small, but those in Fig. 2(c) are larger. In addition, Fig. 2(a) (or Fig. 2(b)) and (c) represents two typical temperature distributions of the c-Si SC (i.e. the FBSs are at the same or different temperatures) and other temperature distribution of the cell under other temperature conditions will be very similar to one of the two distributions. In fact, the temperature distributions in Fig. 2(a) and (b) corresponds largely to those temperature distributions that we try to establish in some standard testing conditions, where the cells under test are needed to maintain a uniform temperature; the temperature distribution in Fig. 2(c) represents the temperature distributions of c-Si SCs in their physical work environments.
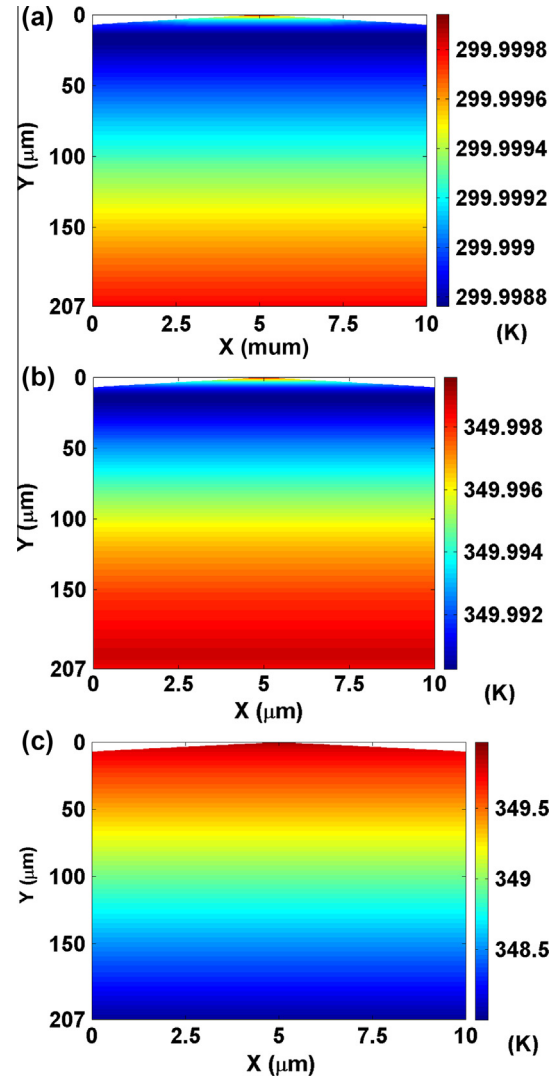

Fig. 2. The temperature distributions of the c-Si SC with different FBS temperatures, where (a) and (b) are the FBSs having the same temperatures of 300 K and 350 K, respectively and (c) is the front surface temperature of 350 K and back surface temperature of 348 K.

Fig. 3 gives a detailed description of the temperature distributions shown in Fig. 2, where the temperature distributions are along two lines parallel to the Y-axis and passing through two points (X = 2.5 μm, Y = 0 μm) and (X = 5 μm, Y = 0 μm). As shown in Fig. 3, the temperature variations along the two parallel lines are same in each figure, but the variations along the line passing through the point (X = 5 μm, Y = 0 μm) can more fully reflect the temperature variations inside the cell; the temperature along the line parallel to the Y-axis will first decrease rapidly and then gradually increase with the Y values increasing for the cell with its FBSs at the same temperature; the temperature will first decrease rapidly and then decrease linearly for the cell with the temperature of the front surface larger than that of the back surface.

3.1.2. The T_g values in the cell's interior under different temperature conditions

According to the temperature variations of the cell's interior, we can divide the temperature distribution in the cell's interior into two temperature regions (i.e. A region and B region), as shown by the dotted ellipses in Fig. 3. These temperature variations can be denoted by T_g values. Due to the non-linear variation of temper-
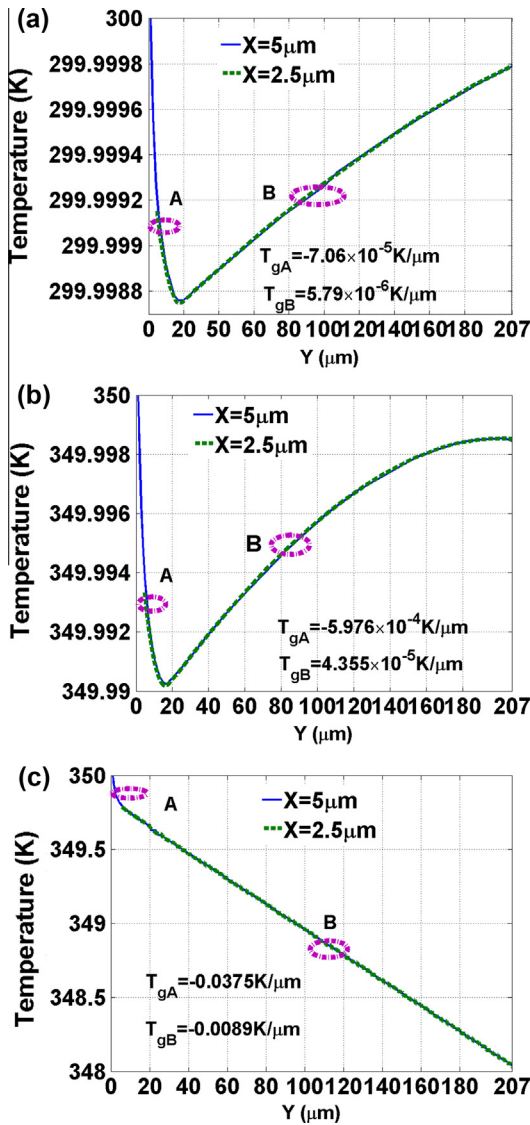
Fig. 3. The temperature distribution profiles of the c-Si SC, where (a) and (b) are the FBSs at the same temperatures of 300 K and 350 K, respectively and (c) is the front surface at 350 K and the back surface at 348 K. A and B denote different temperature regions; T_{gA} and T_{gB} represent the temperature gradients of A and B regions, respectively.

Fig. 4. The temperature distribution profiles of the c-Si SC with the FBSs at different temperatures, where T_{D1}, T_{D2} and T_{D3} denote the temperature difference between the FBSs. (a) and (b) are 300 K and 350 K, respectively.

Table 1
The values of T_g in the different regions of Fig. 3.

T_D (K)	Environmental temperature 300 K		Environmental temperature 350 K	
	T_{gA} (K/μm)	T_{gB} (K/μm)	T_{gA} (K/μm)	T_{gB} (K/μm)
0	-7.06×10^{-5}	5.79×10^{-6}	-5.976×10^{-4}	4.355×10^{-5}
2	-0.0453	-0.0089	-0.0461	-0.0089
5	-0.1099	-0.0222	-0.1111	-0.0222
10	-0.1849	-0.0446	-0.1832	-0.0447

ature with the Y value increasing, T_{gA} and T_{gB} are used to represent the average values of T_g in A region and B region, respectively. As shown in Fig. 3, the values of T_{gA} are larger than those of T_{gB} under different temperature conditions; the T_g values with the FBSs at the same temperature are smaller than those with the FBSs at the different temperature; the T_g values with the FBSs at the different temperatures are determined by the values of T_D between the FBSs.

In order to fully illustrate the features of the temperature distributions of the cell with different T_D values, Fig. 4 gives the temperature distribution profiles of the c-Si SC with the T_D values equal to 2 K, 5 K and 10 K, where the temperature at each Y value represents the temperature at the point ($X = 5$ μm, Y) in the cell's interior. The temperature differences of 0 K, 2 K, 5 K and 10 K will produce the linearly T_g values of 0 K/μm, -0.0097 K/μm, -0.0242 K/μm and -0.0483 K/μm in the cell's interior, respectively, where we regard these values as the ideal values of T_g at different T_D values. As shown in Fig. 4, the change tendency of temperature on each curve is very similar to that shown in Fig. 3 (c). The T_g values for the different regions of the curves given by
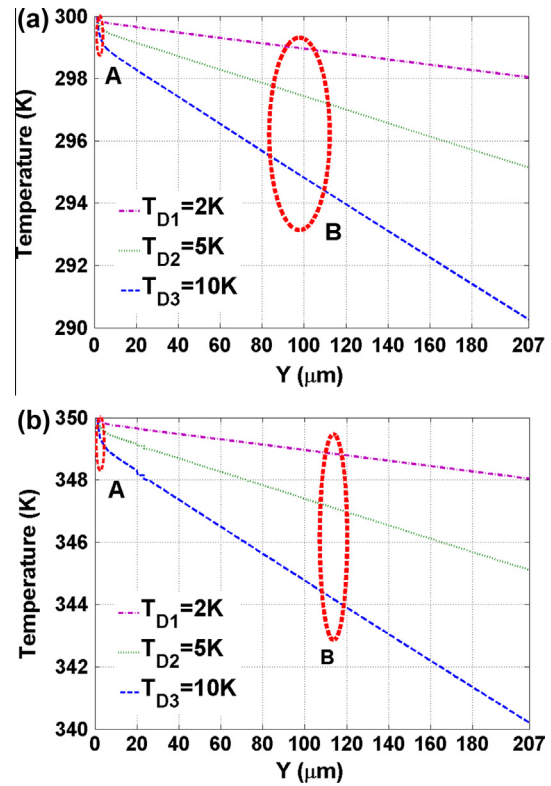
Fig. 4 are listed in Table 1. As shown in Fig. 4 and Table 1, the values of T_{gB} for 350 K are nearly the same as those for 300 K; when the T_D values are lower than 5 K, the absolute values of T_{gA} for 350 K will be larger than those for 300 K, but when the T_D values are equal to 10 K, the absolute values of T_{gA} for 350 K will be less than those for 300 K; the absolute values of dominant T_g values (i.e. T_{gB}) will be smaller than those of the ideal T_g values generated by different T_D values.

3.1.3. The mechanisms for the deviations of the T_{gB} values from their ideal T_g values

The deviations of T_{gB} values from their ideal T_g values (as shown in Figs. 2 and 3) are mainly caused by three thermal mechanisms, i.e. Q_J, Q_C and Q_{PT}. The heat released or absorbed by three thermal mechanisms at 350 K is shown in Fig. 5, where the values of both Q_J and Q_{PT} are denoted by $\frac{Q}{|Q|}\log_{10}(|Q|)$, which represents the logarithm value of heat, but reserves the signs of heat absorbed or released. As shown in Fig. 5, the functions of Q_J and Q_C are to heat the cell, but those of Q_{PT} are mainly to cool the cell; the orders of the heat absorbed and released by Q_J and Q_{PT} are larger than those of the heat released by Q_C; most regions have the same distribu-
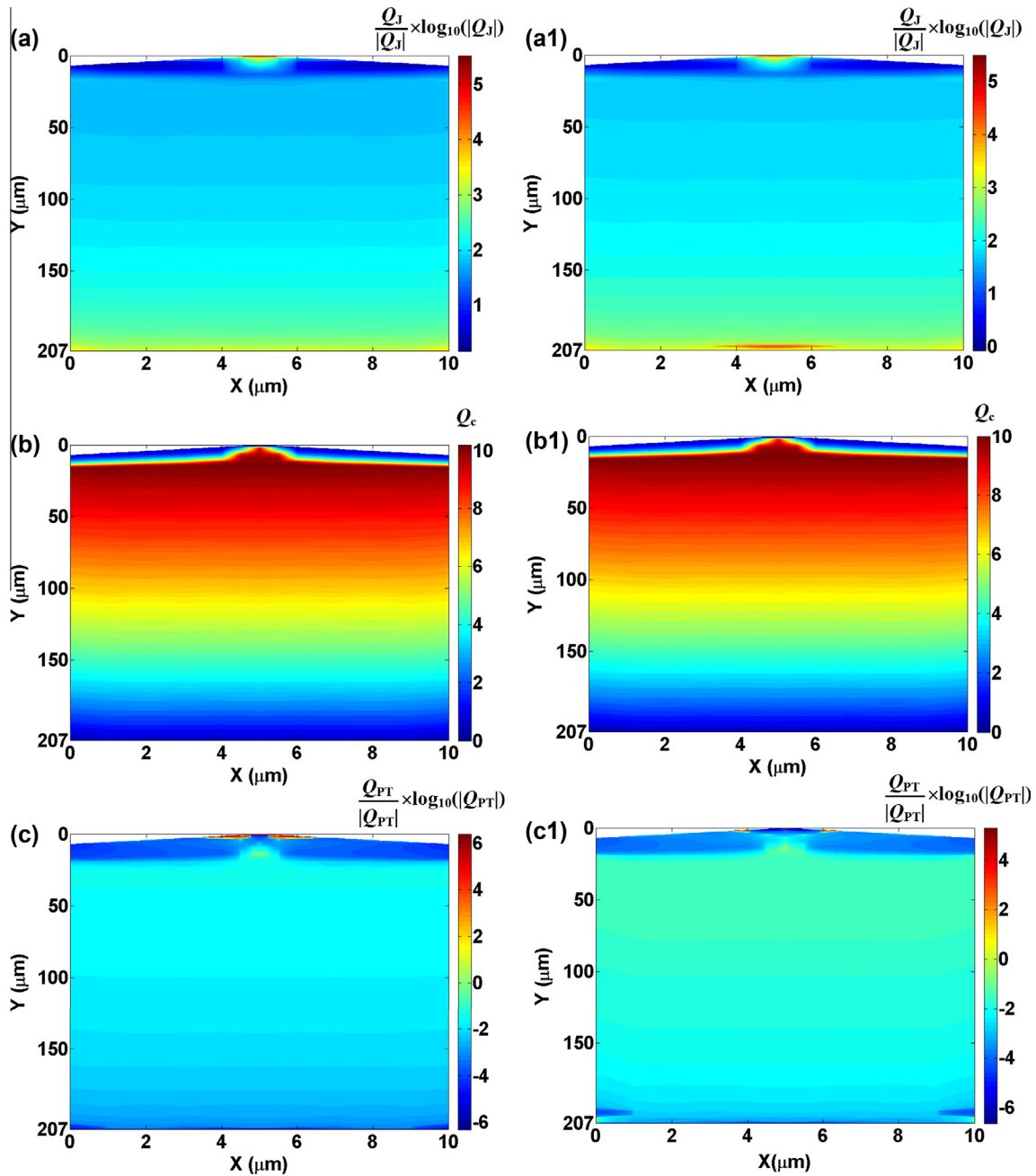
Fig. 5. The distributions of heat released or absorbed by three thermal mechanisms, where (a), (b) and (c) are the cell with the FBSs at 350 K and (a1), (b1) and (c1) are the cell with the front surface at 350 K and the back surface at 248 K. (a) and (a1) are the heat distributions of Q_J; (b) and (b1) are the heat distributions of Q_C; (c) and (c1) are the heat distributions of Q_{PT}.

tions of heat along the X direction, but the distributions of heat have great changes in the regions adjacent to the front surface, especially in those adjacent to cathode; the T_D values between the FBSs will affect the values of heat released and absorbed by three thermal mechanisms, but they have little influence on heat distribution forms.

In order to evaluate the influences of T_D values on the heat released or absorbed by three thermal mechanisms, the profiles of heat along the lines parallel to the Y-axis and passing through the point ($X = 5$ μm, $Y = 0$ μm) in Fig. 5 are shown in Fig. 6. As shown in Fig. 6(a), (b) and (c), the values of Q_J, Q_C, Q_{PT} in the regions away from the FBSs vary approximately linearly with the Y values increasing, but they change drastically in the regions near the FBSs;

the change tendencies of Q_J, Q_C, Q_{PT} at the same environmental temperature are same for the different T_D values. As shown in Fig. 6(d), due to the orders of Q_J larger than those of Q_{PT} in the regions away from the FBSs, the absolute values of Q are positive and increase linearly with the Y values increasing for the different T_D values, but in the regions near the FBSs, the values of Q will become negative, especially in the region adjacent to the front surface, where an broad heat-absorption band appears.

The variations of Q values with the Y values increasing are the main reasons why the change tendencies of T_g values take on the forms shows shown in Figs. 3 and 4, i.e. in the region away from the FBSs, the variations of Q values with the increase of Y values make the T_{gB} values (as listed in Table 1) lower than their ideal
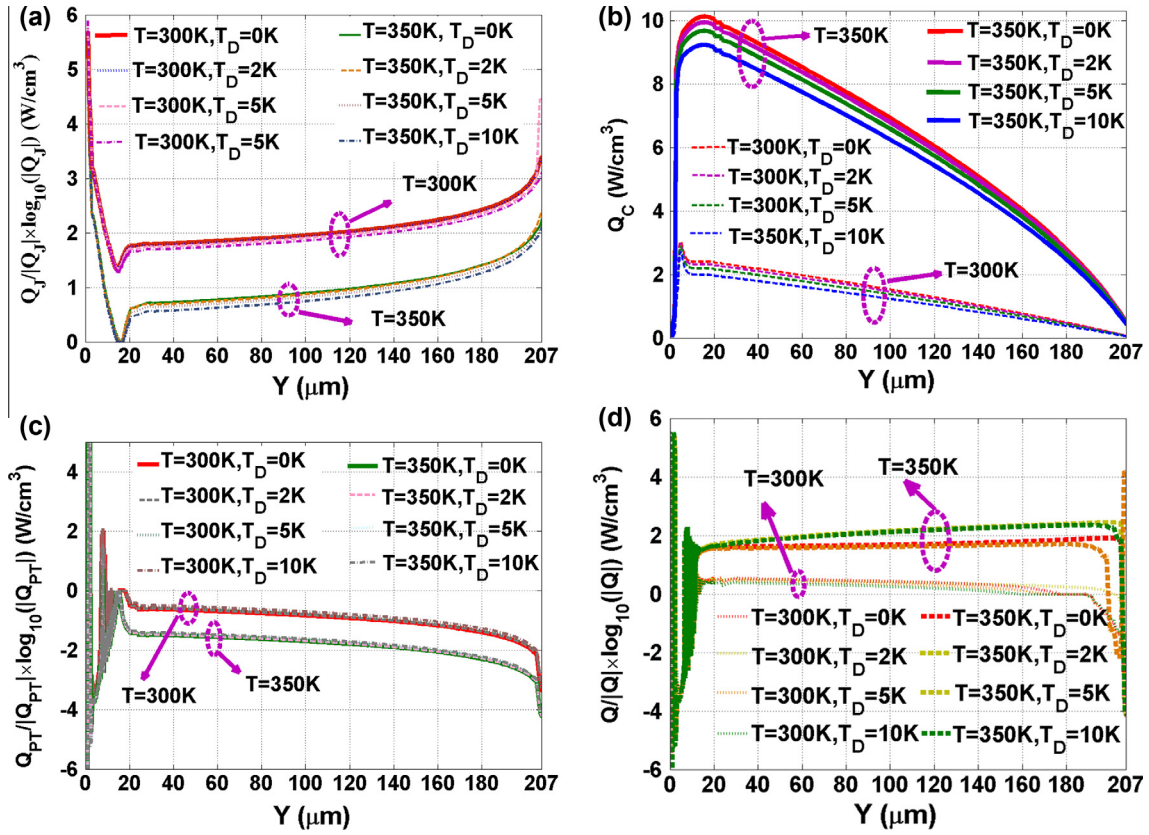
Fig. 6. The profiles of heat distributions along the lines parallel to the Y-axis and passing through the point ($X = 5$ μm, $Y = 0$ μm), where (a), (b), (c) and (d) are the distributions of Q_J, Q_C, Q_{PT} and Q (total heat), respectively. T and T_D denote the environmental temperature and the temperature difference between the FBSs.

T_g values; in the region near the front surface, the temperature will drop abruptly and deviate remarkably from the temperature determined by the environmental temperature and T_D values (as shown in Figs. 3 and 4).

3.2. The influences of environmental temperature and T_D values on the output parameters

The output parameters of the cell varying with temperature are shown in Fig. 7, where T and T_D denote the environmental temperature and temperature difference between the FBSs, respectively. As shown in Fig. 7(a) and (b), the I-V curves at $T_D = 0$ are similar in form for different T values and they gradually approach the J axis with the T values increasing from 250 K to 450 K; at different T values, the I-V curves will gradually move away from the J axis with the values of T_D increasing from 0 K to 10 K; when the T_D values are smaller than 10 K, the influences of T values on the I-V curves are primary, i.e. the T values determine the positions and basic forms of the I-V curves, whereas T_D values will make the I-V curves shift in the horizontal and vertical directions. As shown in Fig. 7 (c) and (d), with the values of T gradually increasing from 250 K to 450 K, the values of $|J_{sc}|$ will increase exponentially from less than 33.4 mA/cm² to about 33.7 mA/cm²; the values of V_{oc} will linearly decrease from larger than 0.7 V to less than 0.4 V; the values of FF will gradually decrease from larger than 84% to about 66%; the values of η will decrease linearly from larger than 20% to less than 10%. Fig. 7(c) and (d) also shows that the effects of T_D are to decrease the values of $|J_{sc}|$ and FF and increase the values of V_{oc} and η.

The variation in rates (VIRs) of the output parameters with T and the deviations of the output parameters with respect to T_D will

be adopted to further evaluate the influence of the temperature on the output parameters. Due to the fact that the curves of V_{oc} and η with the values of T increasing are approximately parallel straight lines for different T_D values, the VIRs of the V_{oc} and η with temperature are same for different T_D values, i.e. the VIRs of V_{oc} values with respect to temperature are about 2 mV/K and those of η values are about 0.072%/K. The curves of $|J_{sc}|$ and FF shown in Fig. 7 (c) and (d) are nonlinear curves and the VIRs of the $|J_{sc}|$ and FF values for different T_D values are shown in Fig. 8(a). As shown in Fig. 8 (a), in the different temperature ranges, the VIRs of $|J_{sc}|$ and FF values vary with T, i.e. The VIRs of $|J_{sc}|$ will first decrease rapidly and then decrease slowly, and also higher at temperature than that at room temperature (300 K), the VIRs of $|J_{sc}|$ values will be lower than about 2.5×10^{-3} mA/cm² K⁻¹; the VIRs of FF values will first decrease slowly and then decrease rapidly and higher at temperature than that at room temperature (300 K), the rates of change of FF values will be lower than -0.08%/K. In the previous studies, Singh et al. have found in theory that the rates of change of $|J_{sc}|$, V_{oc}, FF and η values are 8.57×10^{-3} mA/cm² K⁻¹, 2.04 mV/K, -0.12%/K and 0.0893%/K, respectively (Singh et al., 2008; Singh and Ravindra, 2012); Ghani et al. have theoretically indicated that the rate of change of $|J_{sc}|$, V_{oc} and FF values are 1.8×10^{-3} mA/cm² K⁻¹, 2.2 mV/K and -0.1267%/K, respectively (Ghani et al., 2015); Bensalem et al. have obtained that the rate of change of $|J_{sc}|$, V_{oc} and η values are 2.1×10^{-3} mA/cm² K⁻¹, 2.1 mV/K and 0.063%/K, respectively (Bensalem et al., 2013). It can be seen that the VIR results of the V_{oc} and η values obtained in our work agree well with those obtained by diode models (Singh et al., 2008; Singh and Ravindra, 2012; Ghani et al., 2015; Bensalem et al., 2013), but considering three thermal mechanisms, the results of $|J_{sc}|$ and FF values are more complex than those given by these researchers (Singh
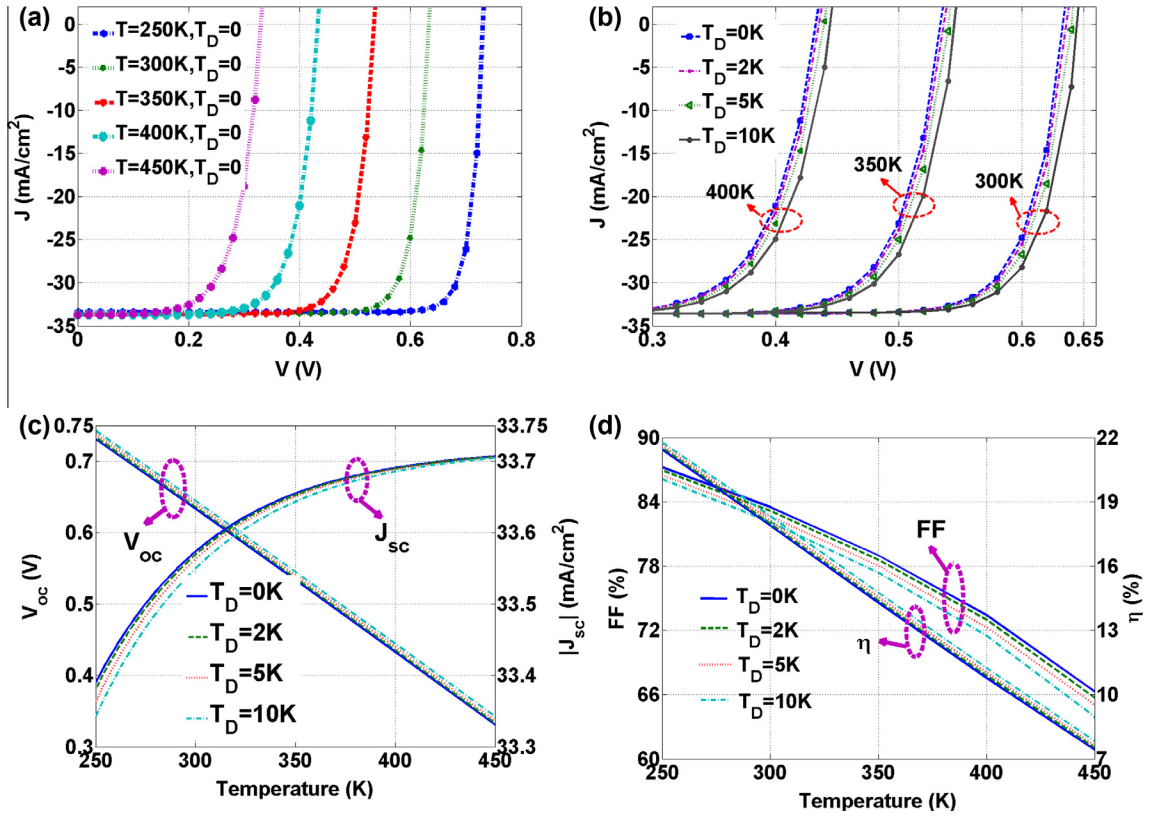
Fig. 7. The variations of the output parameters with temperature, where (a) and (b) are the variations of I-V curves and (c) and (d) are the variations of J_{sc}, V_{oc}, FF and η values. $|J_{sc}|$ is the absolute value of J_{sc}.
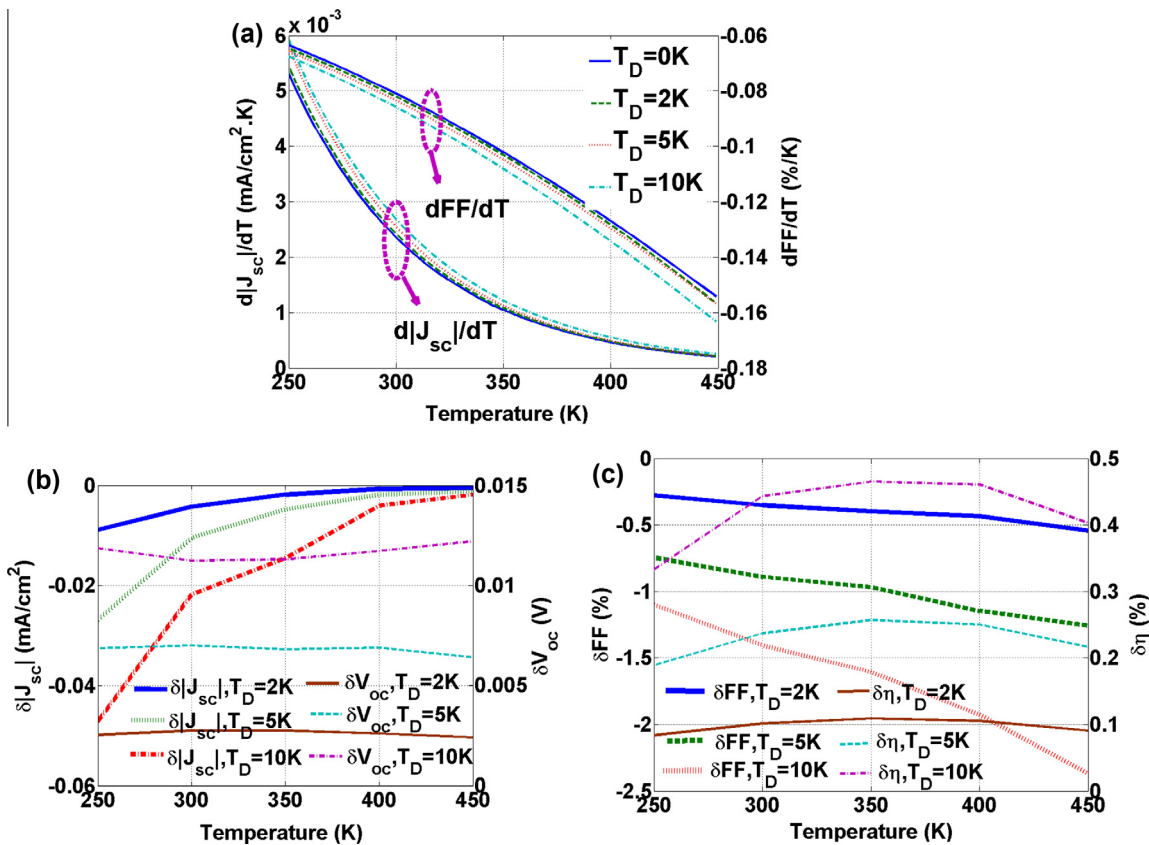

Fig. 8. The variation in rates of the output parameters with temperature (a) and the deviations of the output parameters with respect to T_D values at different T values (b) and (c).

et al., 2008; Singh and Ravindra, 2012; Ghani et al., 2015; Bensalem et al., 2013).

Fig. 8(b) and (c) give the deviation values of $|J_{sc}|$, V_{oc}, FF and η values at the different T and T_D values, where $\delta|J_{sc}| = |J_{sc}|_{Tx1} - |J_{sc}|_{Tx2}$, $\delta V_{oc} = V_{oc\ Tx1} - V_{oc\ Tx2}$, $\delta FF = FF_{Tx1} - FF_{Tx2}$, $\delta\eta = \eta_{Tx1} - \eta_{Tx2}$, respectively and TX1 and TX2 denote T_D = 2 K(/5 K/10 K) and T_D = 0 K, respectively. As shown in Fig. 8(b) and (c), for a specified value of T_D, with the values of T increasing, the absolute values of $\delta|J_{sc}|$ and δV_{oc} will gradually decrease and remain basically unchanged, respectively; those of δFF will gradually decrease; those of $\delta\eta$ will first increase and then gradually decrease. Fig. 8(b) and (c) also shown that for a specified value of T, with the values of T_D increasing, the values of $\delta|J_{sc}|$ and δV_{oc} will decrease and increase, respectively and those of δFF and $\delta\eta$ will decrease and increase, respectively.

4. Conclusion

The influence of the temperature on the output parameters of a typical commercial c-Si solar cell under different temperature conditions is discussed in detail and some important results are listed below:

(1) The temperature distributions of the c-Si SC under different temperature conditions can be divided into two categories (i.e. Fig. 2(a) and (c) given by this work) and the temperature distributions in the cell's interior can be divided into two different temperature regions according to the variations of T_g values.
(2) The T_g values with the FBSs at the different temperature are larger than those with the FBSs at the same temperature and the values of T_D between the FBSs are the dominant factor in determining the T_g values.
(3) The temperature distributions deviated from the ideal temperature distributions in the cell's interior are mainly caused by three thermal mechanisms, i.e. Q_J, Q_{PT} and Q_C. Among these mechanisms, the functions of Q_J and Q_C are to heat the cell, but those of Q_{PT} are mainly to cool the cell; the orders of Q_J and Q_{PT} are larger than those of Q_C in the cell's interior.
(4) The influences of environmental temperature and T_D values on the output parameters of the cell are that: the environmental temperature is the dominant factor in determining the output parameters and functions of T_D values are to produce some deviations for these output parameters.
(5) The effects of T_D are to decrease the values of $|J_{sc}|$ and FF and increase the values of V_{oc} and η.

Conflict of interest

The authors have declared no conflict of interest.

Appendix

Maxwell's curl equations for source-free media in the frequency-domain are

$$\nabla \times \vec{E} = -j\omega\mu\vec{H} \tag{A1}$$

$$\nabla \times \vec{H} = j\omega\varepsilon\vec{E} \tag{A2}$$

where $\vec{E}$ and $\vec{H}$ represent the electric and magnetic field intensities, respectively; ε and μ are dielectric permittivity and permeability, respectively; ω is the frequency of incident light. Eqs. (A1) and (A2) can be discretized in the form of Yee's cell and solved by finite-difference frequency-domain method, as shown by our previous work (Lu et al., 2013).

After solving Eqs. (A1) and (A2), the steady-state distribution of electric field intensity $\vec{E}$ at each grid point in computation area can be obtained. According to Chao et al. (2010) the steady-state distribution of carrier-generation rate can be calculated by

$$\alpha(\omega, \vec{r}) = \frac{\omega \cdot \text{Im}(\varepsilon)|\vec{E}(\omega, \vec{r})|^2}{c \cdot Re[\vec{E}_{inc}(\omega, \vec{r}), \vec{H}^*_{inc}(\omega, \vec{r})]} \tag{A3}$$

$$G_{ph}(\vec{r}) = \int_{\lambda_{min}}^{\lambda_{max}} \frac{\lambda}{hc}I(\lambda)\alpha(\lambda, \vec{r})d\lambda \tag{A4}$$

where $\vec{r}$, ω, λ, h and c are position vector, angular frequency, wavelength, Planck's constant and the speed of light in vacuum; $\text{Im}(\varepsilon)$ is the imaginary part of dielectric permittivity; $\vec{E}_{inc}$ and $\vec{H}_{inc}$ are the electric and magnetic field intensities of incident light, respectively; $\alpha(\omega, \vec{r})$ denotes the absorption coefficient at position $\vec{r}$; I represents the power density per unit wavelength of the solar radiation (ASTM AM1.5 Global tilt).

Assuming that the influences of the steady-state distribution of light field on the carrier transport process are negligible, the behaviors of photon-generated carriers inside a c-Si solar cell will be governed by the following equations

$$\vec{J}_p = -D_p\nabla p - \mu_p p\nabla\Phi \tag{A5}$$

$$\vec{J}_n = D_n\nabla n - \mu_n n\nabla\Phi \tag{A6}$$

$$\nabla\vec{J}_n + (G_n + G_{ph}) - R_n = 0 \tag{A7}$$

$$-\nabla\vec{J}_p + (G_p + G_{ph}) - R_p = 0 \tag{A8}$$

$$\nabla^2\Phi = \rho \tag{A9}$$

$$\rho = -(\Gamma + p - n + G_{ph}) \tag{A10}$$

where Φ, Γ, n, p, $\vec{J}_n$ and $\vec{J}_p$ represent electrostatic potential, net doping concentration, electron concentration, hole concentration, electron current density and hole current density, respectively; D_n, D_p, μ_n, μ_p, G_n, R_n, G_p, R_p are the electron diffusion coefficient, hole diffusion coefficient, electron mobility, hole mobility, electron generation rate, electron recombination rate, hole generation rate, hole recombination rate. Based on the former Yee grid, Eqs. (A1)–(A10) can be discretized and solved by enriched residual free bubble method provided by Simpson et.al. Simpson et al. (2012). Due to the fact that environmental temperature is the main factor influencing the temperature distribution of the cell and heat absorbed or released by different thermal mechanisms will only disturb the temperature distribution, Eqs. (1) and (2) can be solved separately by finite difference method.

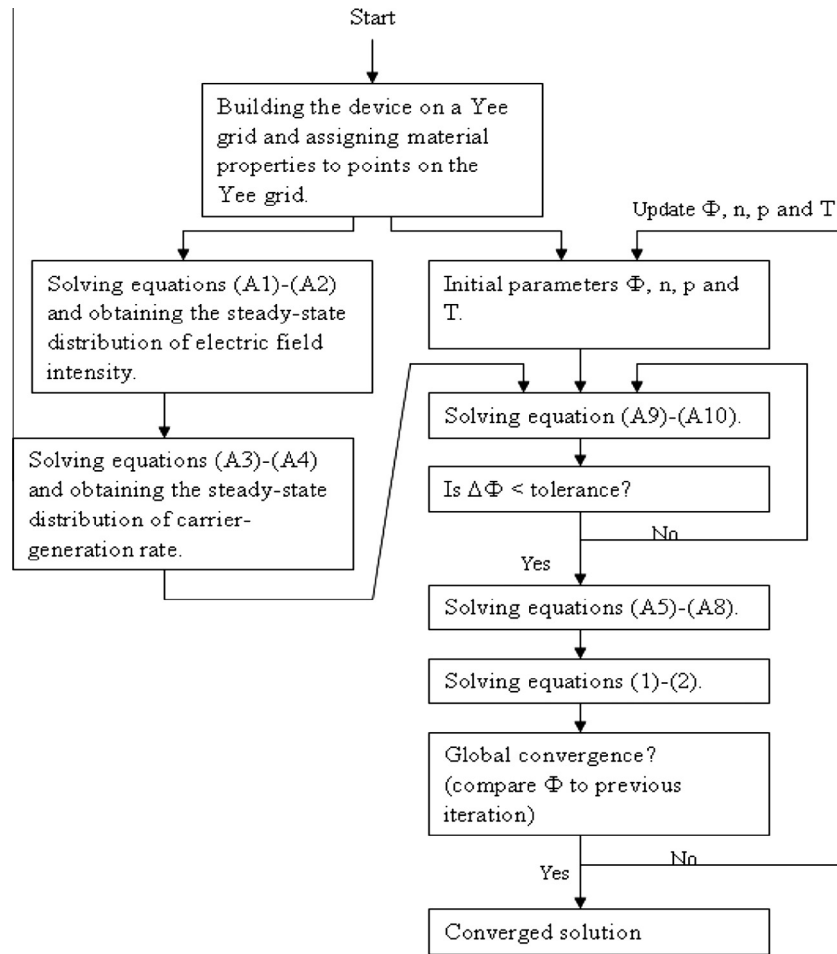Based on the above Eqs. (A1)–(A10) and (1)–(2), the flow chart of the simulation process is shown in Fig. 9.

Fig. 9. The flow chart of the simulation process.

References

Agarwala, A., Tewary, V.K., Agarwal, S.K., et al., 1980. Temperature effects in silicon solar cells. Solid State Electron. 23, 1021–1028.

Ahmad, A.Z., Gunther, B., 2004. Comparative study of thermal flows with different finite volume and lattice Boltzmann schemes. Int. J. Mod. Phys. C 15, 307–319.

Albrecht, J.D., Wang, R.P., Ruden, P.P., et al., 1998. Electron transport characteristics of GaN for high temperature device modeling. J. Appl. Phys. 83, 4777–4781.

Armstrong, S., Hurley, W.G., 2010. A thermal model for photovoltaic panels under varying atmospheric conditions. Appl. Therm. Eng. 30, 1488–1495.

Bensalem, S., Chegaar, M., Aillerie, M., 2013. Solar cells electrical behavior under thermal gradient. Energy Procedia 36, 1249–1254.

Chao, C.C., Wang, C.M., Chang, J.Y., 2010. Spatial distribution of absorption in plasmatic thin film solar cells. Opt. Express 18 (11), 11763–11771.

David, M.R., Paul, P.H., Jesus, G.H., et al., 2005. Photovoltaic solar cells performance at elevated temperatures. Sol. Energy 78, 243–250.

Fan, J.C.C., 1986. Theoretical temperature dependence of solar cell parameters. Sol. Cells 17, 309–315.

Ghani, F., Rosengarten, G., Duke, M., et al., 2015. On the influence of temperature on crystalline silicon solar cell characterization parameters. Sol. Energy 112, 437–445.

Glazov, V.M., Pashinkin, A.S., 2001. The thermophysical properties (heat capacity and thermal expansion) of single-crystal silicon. High Temp. 39 (3), 413–419.

Green, M.A., 2003. General temperature dependence of solar cell performance and implications for device modeling. Prog. Photovoltaics 11, 333–340.

Hosseini, R., Hosseini, N., Khorasanizadeh, H., 2011. An experimental study of combining a photovoltaic system with a heating system. In: World Renewable Energy Congress 2011, Linkoping, Sweden, 2011, May, 8–13.

<http://www.ioffe.ru/SVA/NSM/Semicond/Si/thermal.html>.

<https://en.wikipedia.org/wiki/Heat_equation>.

Indartono, Y.S., Prakoso, S.D., Suwono, A., et al., 2015. Simulation and experimental study on effect of phase change material thickness to reduce temperature of photovoltaic panel. IOP Conf. Ser.: Mater. Sci. Eng. 88, 012049.

Lu, X., Lun, S., Zhou, T., et al., 2013. A low-cost high-efficiency crystalline silicon solar cell based on one-dimensional photonic crystal front surface textures. IOP J. Opt. 15, 075705.

Lycoudes, N.E., Childers, C.C., 1980. Semiconductor instability failure mechanisms review. IEEE Trans. Reliab. R-29, 237–249.

Madra, S., 2004. Carrier depletion effects and heat generation in thermal modeling of GaInP/p-GaAs heterojunction bipolar transistors. In: The Ninth Intersociety Conference on Thermal and Thermo-mechanical Phenomena in Electronic Systems, Las Vegas, USA, June, 1–4.

Simpson, R.N., Borda, S.P.A., Asenov, A., et al., 2012. Enriched residual free bubbles for semiconductor device simulation. Comput. Mech. 50, 119–133.

Singh, P., Ravindra, N.M., 2012. Temperature dependence of solar cell performance-an analysis. Sol. Energy Mater. Sol. Cells 101, 36–45.

Singh, P., Singh, S.N., Lal, M., et al., 2008. Temperature dependence of I-V characteristics and performance parameters of silicon solar cell. Sol. Energy Mater. Sol. Cells 92, 1611–1616.

Slotboom, J.W., 1977. The pn product in silicon. Solid State Electron. 20, 279–283.

Veissid, N., Bonnet, D., Richter, H., 1995. Experimental investigation of the double exponential model of a solar cell under illuminated conditions: considering the instrumental uncertainties in the current, voltage and temperature values. Solid State Electron. 38, 1937–1943.

Wysocki, J.J., Rappaport, P., 1960. Effect of temperature on photovoltaic solar energy conversion. J. Appl. Phys. 31, 571–577.

Xiao, C., Yu, X., Yang, D., et al., 2014. Impact of solar irradiance intensity and temperature on the performance of compensated crystalline silicon solar cells. Sol. Energy Mater. Sol. Cells 128, 427–434.